ADVANCED FUNCTIONAL MATERIALS
www.afm-journal.de

Visible Light Activation of Virucidal Surfaces Empowered by Pro-Oxidant Carbon Dots

Luca Malfatti, Matteo Poddighe, Luigi Stagi, Davide Carboni, Roberto Anedda, Maria Francesca Casula, Barbara Poddesu, Davide De Forni, Franco Lori, Stefano Livraghi, Alessia Zollo, Laura Calvillo, and Plinio Innocenzi**

The scientific community is actively engaged in the development of innovative nanomaterials with broad-spectrum virucidal properties, particularly those capable of producing reactive oxygen species (ROS), to combat upcoming pandemics effectively. The generation of ROS capable of inhibiting viral activity on high-touch surfaces can prove an effective means of reducing pathogenic and viral infections, while avoiding the exacerbation of antibiotic resistance resulting from the extensive use of chemical disinfectants. Carbon dots (C-dots), in particular, are a class of nanomaterials that under specific conditions is able to generate reactive species. They are, therefore, excellent candidates for fabricating light-activated functional antiviral devices. Pro-oxidant C-dots have been developed via microwave synthesis using an amino acid, glycine (Gly), and 1,5-diaminonaphtalene (DAN) as precursors. The formation of C-dots has been obtained by reacting the precursors in microwave using two different acid catalysts, H_3BO_3 or HCl. The HCl catalyst promotes the formation of a copolymer while using H_3BO_3 the precursors preferentially self-condense. The boron-catalyzed samples have shown to contain radical centers whose intensity increases upon illumination by UV and also visible light. They also show the capability of generating singlet oxygen through energy transfer to oxygen molecules when irradiated. The C-dots exhibit effective virucidal activity and have been tested in vitro using two different variants of SARS-CoV-2, the original strain, and Omicron. Antiviral C-dots have been finally used to functionalize a model surface, inducing a strong virucidal activity against the SARS-CoV-2 coronavirus with both ultraviolet (UV) and visible (VL) light.

1. Introduction

The controlled formation of reactive oxygen species (ROS) represents a powerful tool for developing antibacterial and antiviral applications or in photodynamic therapy. ROS naturally form in several biological processes; however, an excess of ROS can cause oxidative stresses in the cells,[1–3] and, more importantly, chemical breakup of different pathogens.[4] On the other hand, ROS and free radicals can disrupt the integrity of several viruses, for instance by breaking the bonds in the lipidic envelope, making ROS-generating nanomaterials a potential effective tool as photoactivated virucidal device. The photosensitized ROS formation, that involves oxygen molecules, depends on the properties of the nanoparticle or molecule that acts as the sensitizer. ROS can be produced through a photoinduced electron transfer, with formation of $O_2^{\bullet-}$ and $HO^{\bullet}$, or via the energy transfer, with the generation of $^1O_2$. In the latter case, the transfer occurs from the sensitizer to O_2 in the ground triplet state and causes its excitation into singlet oxygen, a molecular species that is extremely reactive due to the spin pairing of the two electrons in the π^* antibonding orbitals.

L. Malfatti, M. Poddighe, L. Stagi, D. Carboni, P. Innocenzi
Laboratory of Materials Science and Nanotechnology
CR-INSTM
Department of Biomedical Sciences
University of Sassari
Viale San Pietro 43/B, Sassari 07100, Italy
E-mail: luca.malfatti@uniss.it; plinio@uniss.it

R. Anedda
Porto Conte Ricerche s.r.l.
Strada Provinciale S.P. 55, Loc. Tramariglio, Alghero 07041, Italy

M. F. Casula
Department of Mechanical, Chemical and Materials Engineering
Via Marengo 2 University of Cagliari
Cagliari 09123, Italy

B. Poddesu, D. De Forni, F. Lori
ViroStatics s.r.l.
Viale Umberto I 46, Sassari 07100, Italy

S. Livraghi, A. Zollo
Department of Chemistry and NIS
University of Turin
Via P. Giuria 7, Turin 10125, Italy

L. Calvillo
Department of Chemical Sciences
University of Padua
Via Marzolo 1, Padua 35131, Italy

The ORCID identification number(s) for the author(s) of this article can be found under https://doi.org/10.1002/adfm.202404511

DOI: 10.1002/adfm.202404511

In the design of light-activated antiviral nanosystems, singlet oxygen ($^1O_2$) is the main contributor to virucidal properties.[5] Among the different ROS, singlet oxygen is particularly effective in disrupting the lipids that form the membrane of enveloped viruses. The C=C bonds in the lipids oxidize upon reaction with singlet oxygen, forming hydroperoxyl groups. The lipidic membrane plays a vital role in the fusion of the virion with the cell membrane, and its disruption avoids cell infection.

The use of ROS for antiviral or antibacterial purposes also requires effective control over their functional properties, for instance, activation with light.[6–8] The chemical design of nanosystems that remain noncytotoxic under normal conditions while generating ROS in response to an optical signal is still highly challenging.[9] Several molecules with the capability of producing singlet oxygen have been tested as antiviral photosensitizers, for instance, perylene,[10] porphyrin,[11] and aryl methyldiene rhodanine[12] derivatives. The most severe limitations of such compounds, however, is the poor solubility in water that reduces the possibility to be used as external disinfectants.

Carbon-based nanomaterials are alternative ROS generators. The photo-stimulated generation of $^1O_2$ is well documented for different carbon nanostructures, in particular fullerenes, graphene, carbon nanotubes as well as carbon dots (C-dots).[13] Photoactivated antivirals are ideal for external applications like disinfectants and the creation of biocidal surfaces. C-dots are one of such class of antivirals, due to their ability to generate reactive oxygen species upon UV illumination.[4] Because of their low production cost, high chemical stability, lower environmental impact, and higher solubility in aqueous solutions in comparison to other organic molecules, C-dots are especially valuable for developing biocidal devices.

The photophysical properties of C-dots heavily rely on their surface and core properties, the presence of defects, heteroatoms, and specific functional groups.[14–17] Surface properties also play a significant role in the formation of radical species and the production of singlet oxygen.[9,16] Additionally, the carbon-based matrix has, in general, high biocompatibility and low toxicity, making C-dots suitable for biomedical applications.[18–20]C-dots, in general, also have the capability of direct interaction with the virion[21,22] and they can efficiently adsorb molecular oxygen on the surface, increasing the $^1O_2$ generation yield. These characteristics provide an extra advantage over conventional photosensitizers and single molecules capable of generating singlet oxygen. However, the generation of ROS through photostimulation with ultraviolet (UV) light has certain limitations. In general, UV light has proven biocidal activity but requires special handling procedures and its action is time-limited and ineffective on certain surfaces. For this reason, the possibility of generating ROS through exposure to visible light is of great importance.

In the present work, we have developed a particular type of C-dot produced through microwave treatment of an amino acid together with a polyaromatic molecule, 1,5-diaminonaphthalene (DAN). Glycine is the smallest and most stable amino acid characterized by only one C_α atom and, in aqueous solution, is in the zwitterionic form. In general, the reaction of glycine in hydrothermal conditions is highly dependent on the presence of boric acid to allow the completion of the amidation reactions and extended polycondensation. Through a properly designed polymerization process, glycine can create a carbon-based framework that has the ability to accommodate polyaromatic molecules. This is why the polymeric glycine structure has been chosen to facilitate the formation of sp^2 aromatic molecular units and extended polyaromatic structures when reacted with DAN. Additionally, glycine acts as a nitrogen-doping source, which follows a well-established strategy observed in other DAN-based C-dots.[23–25] DAN, in fact, exhibits a strong tendency to oxidation, leading to an increased presence of oxygen-containing functional groups, including ketonic carbonyls that further promote the generation of ROS.[26] In this study, we have successfully synthesized two types of C-dots able to generate ROS via photoactivation. They have been obtained using two different acid-catalyzed reactions: the first promoted by a Lewis acid such as H_3BO_3, and the second by a strong protic acid, HCl. We have evaluated the antiviral efficacy of these C-dots against the SARS-CoV-2 coronavirus, both in the form of liquid dispersion and when attached to a surface. We have carefully characterized the structure of the C-dots, identifying the various parameters that affect the properties of the C-dots, such as their size, surface chemistry, and then studied their functional properties. As a proof of concept, we have designed a C-dot-functionalized silicon wafer as a prototype for visible light-activated virucidal surfaces.

2. Results and Discussion

To synthesize C-dots with specific functional properties a careful design, which takes into account the requirements of the application, is required. The use of C-dots as antiviral agents must ensure photo-activated ROS emission under both UV and visible light (VL) excitation. It is also crucial that the nanoparticles do not exhibit any cytotoxicity. We have characterized the structure of the nanoparticles, their functional properties including their virucidal capability and finally developed a proof-of-concept antiviral active surface.

2.1. C-dot Structure

C-dots composed of glycine (Gly) and 1,5-diaminonaphtalene (DAN) have been prepared using a microwave treatment and two different catalysts: H_3BO_3 and HCl. The resulting nanoparticles have been indicated as GDB and GDH, respectively. Gly and DAN have been chosen based on specific criteria: Glycine is a noncytotoxic amino acid that can thermally polymerize and form nanoparticles when catalyzed with boric acid,[27] DAN, instead, is an aromatic molecule that can promote ROS formation, particularly if partially oxidized.[21–23] Both precursors, when co-reacted in a microwave, generate nanometer-sized particles (**Figure 1a**).

The transmission electron microscopy (TEM) images indicate that the C-dots vary in shape and size depending on the acid used during synthesis. (Figure 1b). The C-dots synthesized using H_3BO_3 display a spherical shape with a size distribution peaking around 18 nm. In comparison, the C-dots synthesized by HCl appear as small spherical nanoparticles of high electronic contrast surrounded by polymeric shells with irregular shapes and lower electronic contrast. The dimension of these C-dots (indicated by the white arrows in the magnification inside Figure 1c) is less

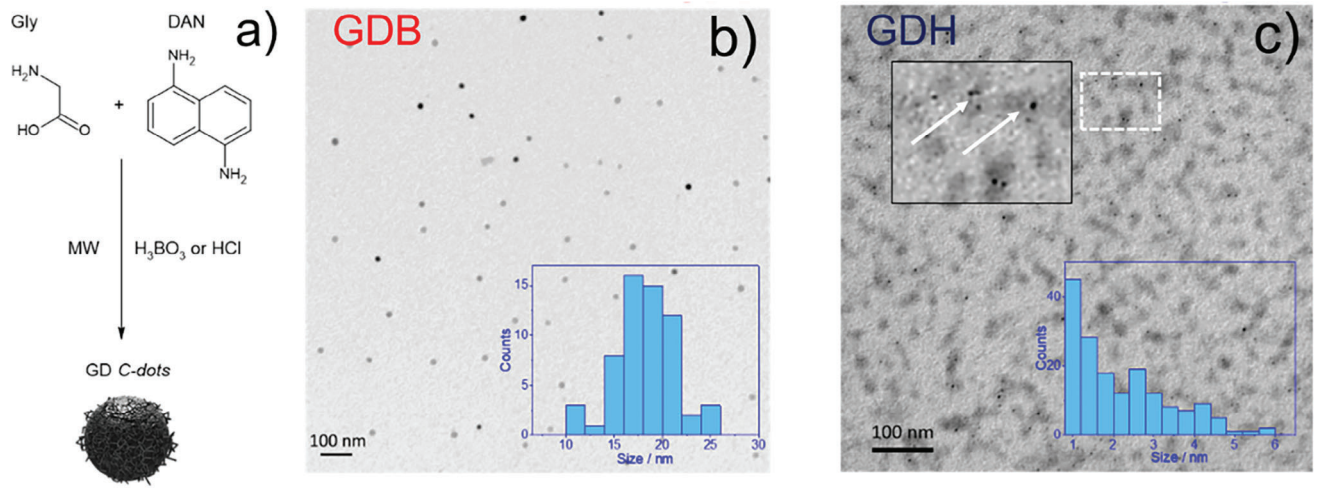

Figure 1. a) Scheme of the GD (Glycine-DAN) C-dot fabrication. Gly and DAN precursors are co-reacted in a microwave with the addition of a catalyst, HCl (GDH) or H_3BO_3 (GDB). b) TEM images of GDB C-dots; c) TEM images of GDH C-dots. An image magnification shows the high-contrast C-dot cores (indicated by the white arrows). The GDB and GDH size distributions are shown in the insets.

than 6 nm. The comparative analysis of the two samples shows that the choice of the catalyst governs the structure even when the particles are synthesized from the same precursors.

To get a better insight of the C-dot structural properties a combination of various techniques has been applied. **Figure** 2a shows the X-ray diffraction (XRD) patterns of GDB and GDH, along with Gly and DAN precursors taken as references.

The XRD patterns of the C-dots exhibit numerous reflections associated with the organized arrangement of the crystalline Gly and DAN precursors (Figure 2a). Notably, GDB displays distinctive alpha-glycine peaks (P21/c, reference code 00-002-0687), which are clearly detected even after 48 h of dialysis. The diffraction peak intensities, however, differ with respect to the Gly reference sample, indicating a structural reorganization of the residual monomeric glycine within the dots. The most intense DAN diffraction peaks (reference code 96-220-3126) no longer appear in GDB. This can be explained by the hypothesis of a reaction of DAN molecules to form amorphous polymer structures. The GDH sample shows four distinct diffraction peaks at 23.5, 27, 39, and 46°, which do not find a precise correspondence in the diffractograms of the precursors.

Figure 2b shows the Fourier-transform infrared (FTIR) spectra of GDH and GDB in the 1800 and 1000 cm^{-1} range. The extended spectra between 4000 and 400 cm^{-1} are reported in Figure S1 (Supporting Information). The spectra are characterized by the superimposition of the main vibrational modes of Gly and DAN. The corresponding -NH_2 scissoring and wagging modes are located at 1626 and 766 cm^{-1}. Aromatic C═C stretching vibrations typically occur in the 1450—1600 cm^{-1} range. In GDB, distinctive features emerge from the overlapping of COO and NH_2 bending and stretching modes, located between 1600 and 1575 cm^{-1}, with a prominent band ≈ 1500 cm^{-1} stemming from the asymmetrical bending and rocking of the NH_3^+ group. The range between 1500 and 1250 cm^{-1} primarily corresponds to CH_2 stretching and bending bands, while two additional modes at 1125 and 1042 cm^{-1} persist and can be attributed to C—O and C—N stretching, respectively. In GDH, distinctive absorptions corresponding to the vibrational modes of the DAN monomer are observed. This is particularly noticeable in the spectral range between 1600 and 1500 cm^{-1}, and at lower frequencies between 1200 and 1000 cm^{-1}, where the C═O and C—N groups of Gly are less prominent compared to GDB. In general, the infrared

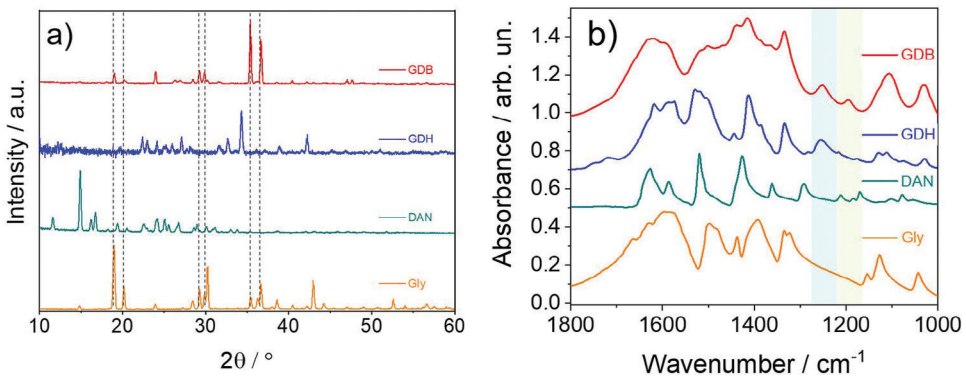

Figure 2. a) XRD patterns of Gly, DAN, GDB, and GDH. b) FTIR absorption spectra in the 1800–1000 cm^{-1} interval of Gly, DAN, GDB, and GDH samples.

spectra, characterized by broadening and reduction in the detail of the characteristic monomer vibrational modes, represent a signature of the polymeric nature of both C-dots.[28] Additionally, the spectra suggest that the GDB dots contain a comparatively higher proportion of Gly in both its monomeric and linear polymeric forms. Lastly, two vibrational modes at 1252 and 1195 cm^{-1} are noteworthy, as they do not appear in the precursor compounds. The 1195 cm^{-1} band is detected in both C-dots, whereas the 1252 cm^{-1} vibrational mode is exclusively found in GDB. This component is tentatively attributed to Aryl-O-R ether bonds, probably formed by condensation between DAN and Gly without amide bond formation. The second is assigned to Aryl—OH—type bonds, which can form as an effect of a strong oxidative process of DAN.

The GDH and GDB samples have been also analyzed by nuclear magnetic resonance (NMR) spectroscopy. The ^{1}H-NMR spectrum of GDH (**Figure 3a**) shows a well-defined pattern whose signals are assigned to a compound (DAN-Gly_2) formed by the reaction of DAN and Gly precursors in a 1:2 ratio (**Scheme 1**).

The singlet at 3.64 ppm, integrating for 4H, is assigned to the four methylene protons of Gly (bonded to carbons 15/19 of DAN-Gly_2 structure of Figure 3a) that are detected at lower chemical shifts with respect to free Gly (expected at 3.09 ppm). The doublets lying at 6.72, 7.29, and the triplet at 7.10 ppm can be unambiguously attributed to the six aromatic protons of DAN (Figure S2, Supporting Information). Based on their multiplicity and ^{1}H-COSY correlations (Figure S3, Supporting Information), they must be bonded to carbons 6/9, 4/7, and 5/8 in DAN-Gly_2 (see left inset in Figure 3a).

Also, these DAN signals are downshifted compared to the free molecules, in particular, those attributed to protons closer to the amide groups. The integral ratio indicates that each amino group of DAN reacts with the carboxylic group of Gly forming an amide bond. The reaction produces the symmetric molecule shown in Figure 3a. The broad signal lying at 8.35 ppm can be attributed to the N-H amidic protons that, together with the absence of the signals at 5.4 ppm of free -NH_2 of DAN, confirms the formation of the amide bonds. The terminal Gly does not show any signal related to free -NH_2 (<3.0 ppm). The protonation by HCl downshifts, in fact, the signal of the corresponding ammonium salt to 8.12 ppm.[29] Given the broad nature of -NH signals, it is reasonable to assume that both the amidic -NH and the protonated -NH_3^+ of the terminal Gly moieties overlap under the broad signal centred at 8.35 ppm. This assumption is further confirmed by the integral of this signal, which counts for 8H (6 for the two protonated GLY and 2 for the two amidic moieties). The evidence produced by the 1D ^{13}C NMR spectra and the 2D ^{1}H-^{13}C HMBC map (Figure S4a,b, Supporting Information) supports the previous hypothesis by showing a correlation between the signal at 169.33 ppm, that can be ascribed to the carbonyls of the amide (13/14), and the 2-bonds apart methylene protons of Gly (bonded to carbons 15/19 and whose proton signal lies at 3.64 ppm). In contrast, there is no clear evidence of free Gly, given the absence of the very diagnostic signal of free -COOH (δ_H > 9 ppm and δ_C > 171 ppm). This was expected since the sample was dialyzed against water. The other signals on the ^{13}C NMR spectrum (143.69, 124.98, 124.53, 111.47, and 109.10 ppm), attributed to the aromatic carbons of DAN, correspond to the carbons 1/10, 2/3, 5/8, 4/7 and 6/9 on the structure reported in Figure 3a. Very weak signals at 3.96 and 4.40 ppm can be assigned to α-CH_2 of terminal Gly molecules. The presence of minor aromatic products is suggested by the amplified signals between 6.5 and 7.5 ppm (right inset Figure 3a) and confirmed by both the ^{1}H-^{13}C HSQC and HMBC maps (Figures S4b and S5, Supporting Information). The appearance of a broad band that emerges from the flat baseline (4 – 10 ppm), in the ^{1}D proton spectra of GDH (see inset **Figure** 3a), suggests that the sample also contains macromolecular aggregates of hydrocarbons, which cannot be resolved by liquid-state NMR due to slow reorienting motions with respect to the magnetic field. The carbonaceous core is, however, surrounded by a major product, that is, DAN-Gly_2, derived from the amidation reaction of the aniline groups of DAN with the carboxylic moieties of Gly, activated by hydrochloric acid.

NMR analysis of GDB leads to different considerations, given its articulated resonance pattern shown in Figure 3b. The GDB nanoparticles have been obtained from a reaction catalyzed by boric acid, a well-known Lewis acid, which has been used in stoichiometric amounts. Boric acid promotes the complete conversion of DAN into reaction products, while unreacted Gly is still present. Interestingly, the GDB pattern does not show any signal that can be directly correlated with the unreacted DAN precursor. This result suggests that all the 1,5-diamino-naphthalene undergoes self-polymerization to form oligomeric structures through an oxidative pathway. On the contrary, the signals from the methylene proton of residual free Gly can be detected both in the 1D proton spectrum (3.01 ppm) (Figure 3b) and confirmed by the correlation of this signal with ^{13}C resonances (HSQC at 41.9 ppm attributed to CH_2-NH_2; HMBC cross peak at 168-3.01 ppm attributed to H_2N-CH_2-COOH, Figure S6a,b, Supporting Information). According to the integrals of the HSQC cross-peaks (3.02/41.9 ppm and 3.3-3.46/43.4 ppm), we estimated that ≈ 20% of the Gly in GDB is not polymerized.

The remaining Gly has reacted through different pathways catalyzed mainly by boric acid, and the resulting species can be identified by several signals related to the respective methylene protons. The broad proton signal at 3.33 ppm is assigned to the -NH_2 group of free Gly; however, this signal overlaps with those of the methylene protons of at least three forms of glycine derivatives, which can be detected as HSQC cross peaks around 43 ppm (Figure S6a, Supporting Information). The broad signals at 6.55 and 6.79 ppm in the COSY spectrum (Figure S7, Supporting Information) show that some of these methylene groups couple with downfield shifted signals of -NH protons (3.34/6.55 and 3.46/6.79 ppm), compatible with -CH_2-NH-X moieties. This finding suggests the presence of Gly species attached to a heteroatom X, such as Boron, as expected from a reaction with boric acid. The NMR signals lying in the range between 4.10-3.45 ppm can be attributed to methylene protons of poly-glycine species or other secondary products. The HMBC correlation at 3.33 – 171 ppm is ascribed to a long-range scalar coupling between amine protons and carbonyl carbons of Gly (free terminal -COOH). However, we could not detect free carboxylic protons in the ^{1}H spectrum (>8.5 ppm). Free Gly retains some reorientation freedom even if it is reasonably buried inside the polymeric strands and linked by non-covalent bonds.

With regards to the DAN moieties, it is possible to hypothesize that the signals in the 7.0 – 7.7 ppm range of the HSQC and HMBC maps belong to aromatic protons and, in particular, to

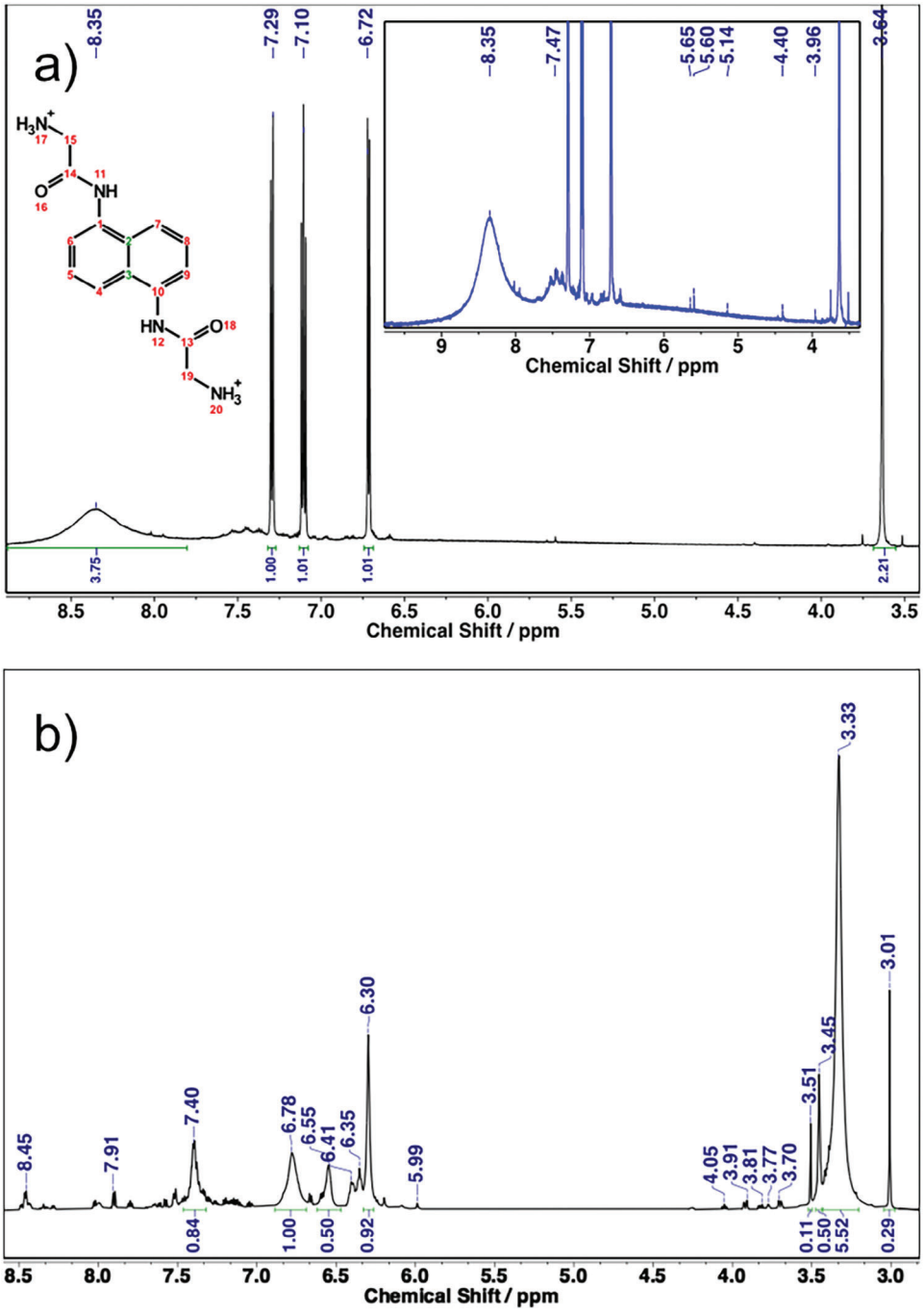

Figure 3. a) ^{1}H NMR spectrum of GDH. The inset shows an magnification of the signals. The structure of the DAN-Gly$_2$ compound with the numbers to indicate the different positions of C atoms is shown inside the Figure on the left. b) ^{1}H NMR spectrum of GDB.

the benzenoid protons of oligomeric structures of poly-DAN. The polymerization likely takes place through the formation of a quite unstable radical cation that immediately couples with a neutral 1,5-DAN monomer to produce a neutral radical and a protonated monomer species, which, after undergoing a series of transformations, produces an aromatic dimer of DAN. The latter can take part in another oxidation cycle to form a trimer until an oligomeric structure is reached (**Scheme 2**). A similar polymerization product was hypothesized by Pierre et al. that obtained poly-1,5-DAN through an electro-oxidative process.[30] The presence of boric acid favors a similar oxidation path, activating the DAN and stabilizing a spontaneous formation of radical DAN species. Interestingly, the microwave-assisted reaction catalyzed by Lewis acid leads toward a self-polymerization of the precursors (i.e., poly-Gly and poly-DAN) rather than a reaction between them, as seen for the reaction catalyzed by a protic acid.

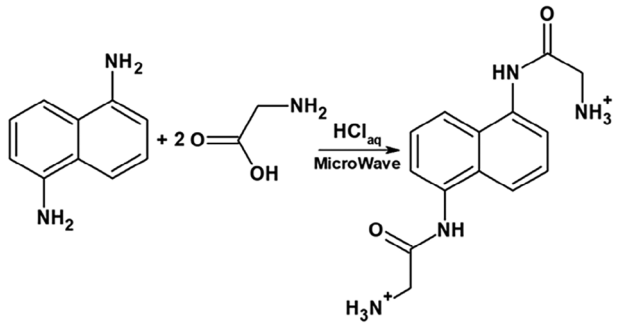

Scheme 1. Microwave-assisted reaction pathway of DAN with two Gly molecules catalyzed by aqueous HCl to form a DAN-Gly_2 compound.

This outcome can be justified by considering the well-known ability of boric acid to promote preferentially the polyamidation of amino acids.[31]

The spectroscopic data show that the nanoparticles obtained using HCl or H_3BO_3 as catalysts have quite different structures, even starting with the same precursor. In the GDH dots, the complete reaction of DAN with the amino acid gives DAN-Gly macromolecular polymeric structures; in the GDB, the two precursors self-polymerize, giving extended poly-DAN macromolecules, and Gly polymers of shorter length, mostly oligomeric, in nature.

X-ray photoelectron spectroscopy (XPS) measurements have been performed to identify the different C and N species and to confirm the structures deduced from the NMR measurements. The C 1s region of GDH can be fitted with five components at 284.4, 285.2, 286.0, 287.7, and 289.0 eV, attributed to C═C, C─C, C─N, C═O, and COOH groups, respectively (Figure 4a).

The presence of the component at 284.4 eV supports the hypothesis of the formation of macromolecular aggregates with graphitic-like structure when HCl is used, while the very low intensity of the COOH component confirms that unreacted Gly units are not present. The N 1s region (Figure 4b) contains two components at 399.5 eV, related to the presence of terminal -NH_2 groups, and at 400.5 eV, assigned to the amide groups (C─NH─C) created by the reaction of Gly with DAN (Scheme 1).[32,33] Unexpectedly, it also shows a component at lower binding energy (398.5 eV) that could be attributed to C─N═C species, coming from the tautomeric equilibrium formed between the amidic and imidic forms.[34–36]

GDB samples have shown some differences in the XPS spectra, which suggest the presence of other species when boric acid is employed in the synthesis (as shown in Figure 4c). In such cases, the C 1s region does not present the 284.5 eV component associated with the formation of a graphitic-like structure, but instead shows a component at 284.9 eV, characteristic of C sp^3 in organic molecules or compounds. This result agrees with the presence of Gly, Gly oligomers, and Gly-boric acid derivatives. The presence of boron, as confirmed by the XPS survey (Figure S8, Supporting Information), suggests that Gly species react with boric acid, which is also in agreement with the NMR results. Additionally, the presence of unreacted Gly is confirmed by the detection of the 289.0 eV component related to COOH groups.

The analysis of the N 1s region of GDB is more complex due to the presence of five different components, at 398.5, 399.5, 400.5, 401.5, and 402.7 eV (Figure 4d). The components at 399.5 and 401.5 eV are attributed to -NH_2 and -NH_3^+ species, characteristic of the unreacted Gly.[27,28,37] The component at 400.5 eV, assigned to the amide bond, confirms the formation of Gly oligomers. The components related to the corresponding C═N^+(H)─C and C═N─C species overlap with the components at 401.5 and 398.5 eV, respectively.[30] The component at 398.5 eV, which increases with DAN content (Figure S9; Table S1, Supporting Information) can also be assigned to C─N═C species present in the poly-DAN structures observed by NMR. In addition, a small component associated to -NO species is observed, likely due to the oxidation of amino groups of DAN.

2.2. Characterization of the Functional Properties

The content of carbon radical centers (C•) in the C-dots and the photoinduced production of singlet oxygen have been investigated by two sets of Electron Paramagnetic Resonance (EPR) measurements. In the first set of experiments (**Figure 5a–d**), solid state EPR measurements have been carried out on C-dots placed in a high vacuum cell, as vacuum conditions are crucial to prevent the influence of molecular oxygen, which is a paramagnetic molecule itself. The EPR measures have been done in three conditions: dark, upon exposure to UV, or blue VL.

A weak isotropic signal at $g = 2.004$, attributed to carbon radical species (C•), in an approximated concentration of 4.0×10^{14} spins g^{-1},[38,39] characterizes the GDB EPR spectrum. The spectrum also shows the presence of minor signals that resonate at $g = 2.054$, $g = 2.030$, and $g = 1.978$ due to unassigned species. The abundance of carbon radical species (C•) depends on the irradiation conditions as shown by the changes in the signal at $g = 2.004$. Upon irradiation by UV the C• signal increases, indicating the photoinduced formation of radical centers. An increase is also observed by illumination with VL even it is smaller compared to that induced by UV irradiation (Figure 5a,b). The same change is detected in both vacuum and oxygen atmospheres while the different measurement conditions do not affect the other minor features in the GDB spectrum. Finally, once interrupting the light exposure, the original intensity of the C• signal is restored after ≈ 60 min (Figure S10, Supporting Information).

In the second set of experiments, the formation of singlet oxygen under blue light exposure has been monitored in solution using the 4-oxo-TEMPH molecules as a trapping agent. This compound reacts with singlet oxygen to form the paramagnetic 4-oxo-TEMPO adduct (**Scheme 3**), which can be easily detected by EPR.[40]

For the GDB sample, the spectra, recorded at 5, 30, and 60 min, display a monotone variation of the EPR integrated area as a function of the exposure time that is correlated to the formation of singlet oxygen (Figure 5e). Moreover, the comparison between two GDB samples prepared with different DAN molar ratios (GDB with 1:1 and GDB_05 with 1:0.5 Gly:DAN molar ratios) suggests that the formation of singlet oxygen is linearly correlated with DAN concentration (Figure 5f). A lower content of DAN produces less singlet oxygen, the difference also increases with the time.

Remarkably, the EPR spectrum of the DAN molecule also shows the same signal attributed to C• species with an intensity

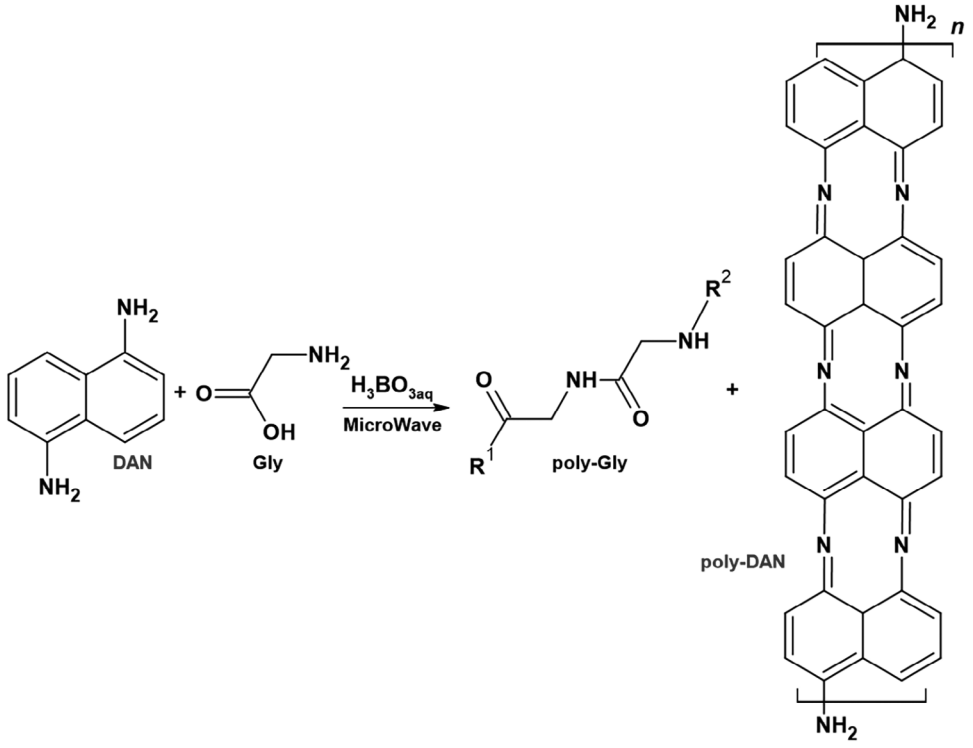

Scheme 2. Microwave-assisted reaction pathways of DAN to poly-DAN and Gly to poly-Gly, catalyzed by aqueous boric acid.

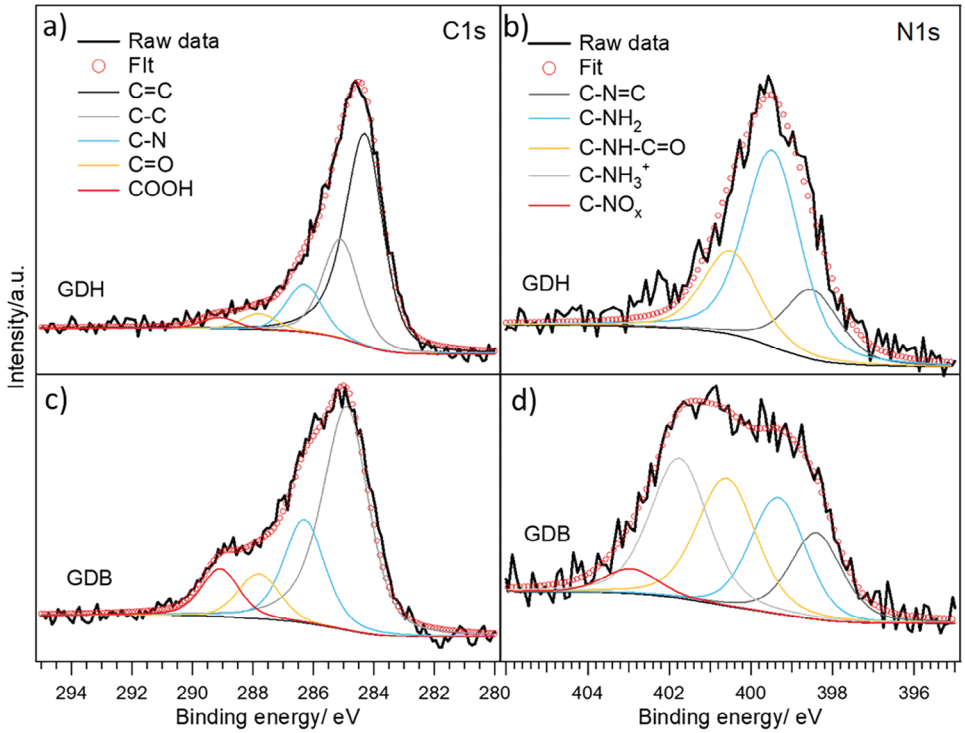

Figure 4. C1s and N1s peaks of XPS spectra measured on GDH (a and b) and GDB C-dots samples (c and d).

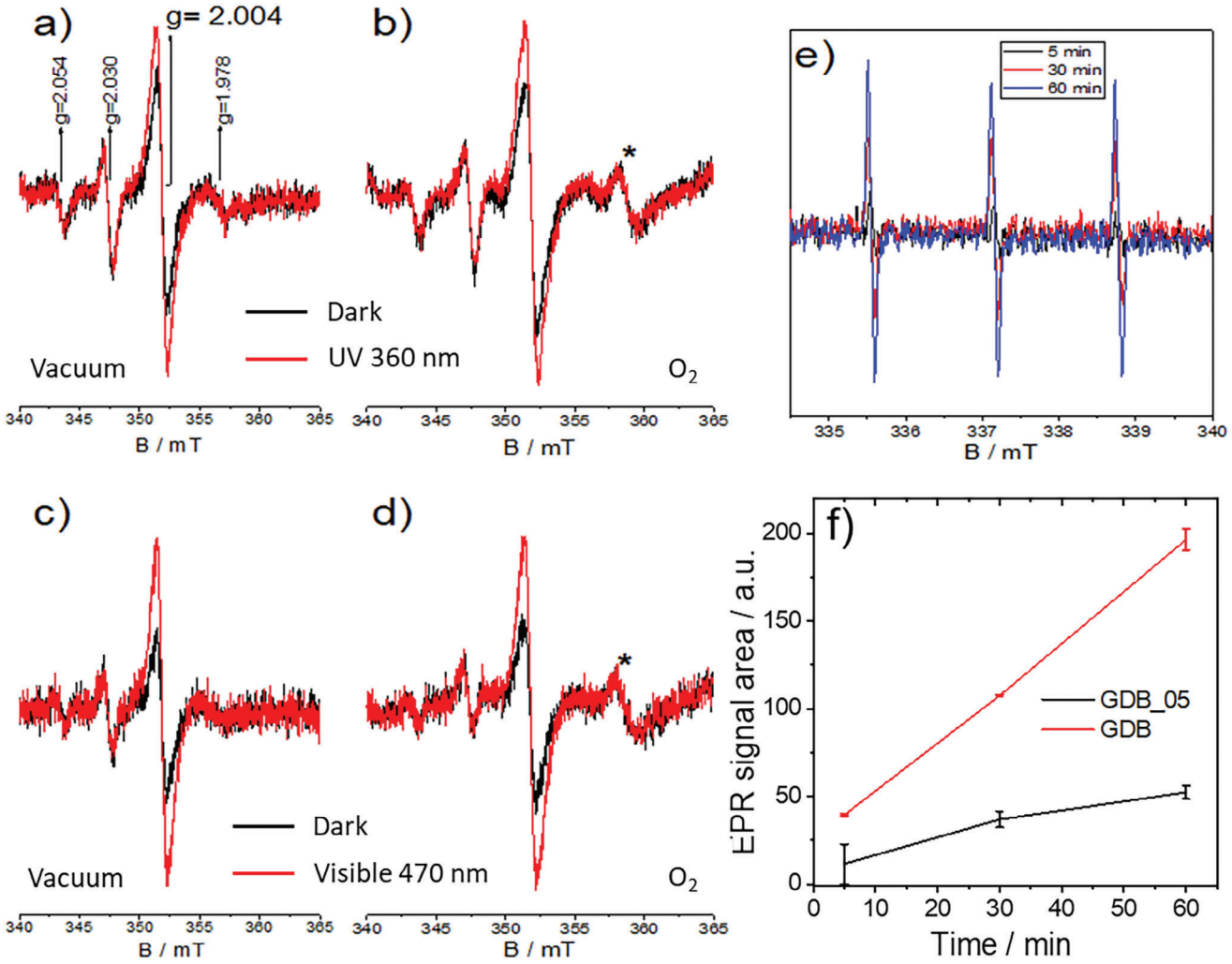

Figure 5. a) EPR spectra of GDB measured before (black spectrum) and after irradiation (red spectrum) with UV light (360 nm) in vacuum for 8 min. b) The same EPR measures shown in a) are repeated in O_2 atmosphere (20 mbar). c–d) The EPR spectra recorded under VL at 470 nm in vacuum (c) and in O_2 (d). The signal marked with * is due to the presence of O_2 in the measurement cell. e) EPR spectra of 4-oxo-TEMPO in a GDB suspension exposed to VL (470 nm) for 5, 30, and 60 min. f) Singlet oxygen formation measured by the EPR signal area when exposing to VL (470 nm) the GDB (red curve) and GDB_05 samples (black curve) for increasing times (5, 30, and 60 min). The lines are a guide for eye.

similar to that of GDH C-dots, indicating a concentration in the 10^{14} spins g^{-1} range. The signal, however, is not sensitive to UV or VL (Figure S11, Supporting Information). Finally, DAN molecules are not capable of producing singlet oxygen in the same condition as GDB.

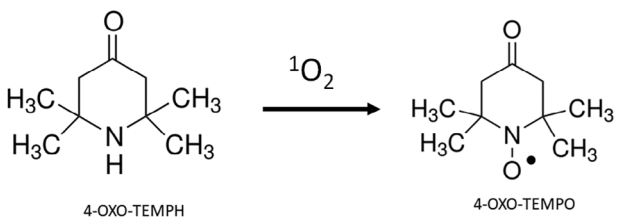

Scheme 3. Formation of the paramagnetic 4-oxo-TEMPO adduct from the 4-oxo-TEMPH molecule in the presence of singlet oxygen.

The EPR spectra of GDH exhibit a signal assigned to C• similar to what detected in the GDB sample (g = 2.003), but no traces of the other minor spectroscopic features are observed (Figure S12a, Supporting Information). Moreover, in these C-dots the C• signal has a significantly higher intensity (5.4×10^{17} spins g^{-1}). However, this species does not display any photoresponse if exposed to UV or blue light, in vacuum or in the presence of oxygen (Figure S12b–d, Supporting Information).

The EPR characterizations yield a crucial finding, indicating that carbon radical species do not play a significant role in light-induced singlet oxygen generation. The behaviour of the C• signal under irradiation in fact do not change in presence of oxygen in solid state EPR measurements suggesting that no direct interaction with O_2 occurs. Moreover, comparing the EPR features of the GDB and GDB_05 samples (Figure S13, Supporting Information) the ability to produce singlet oxygen

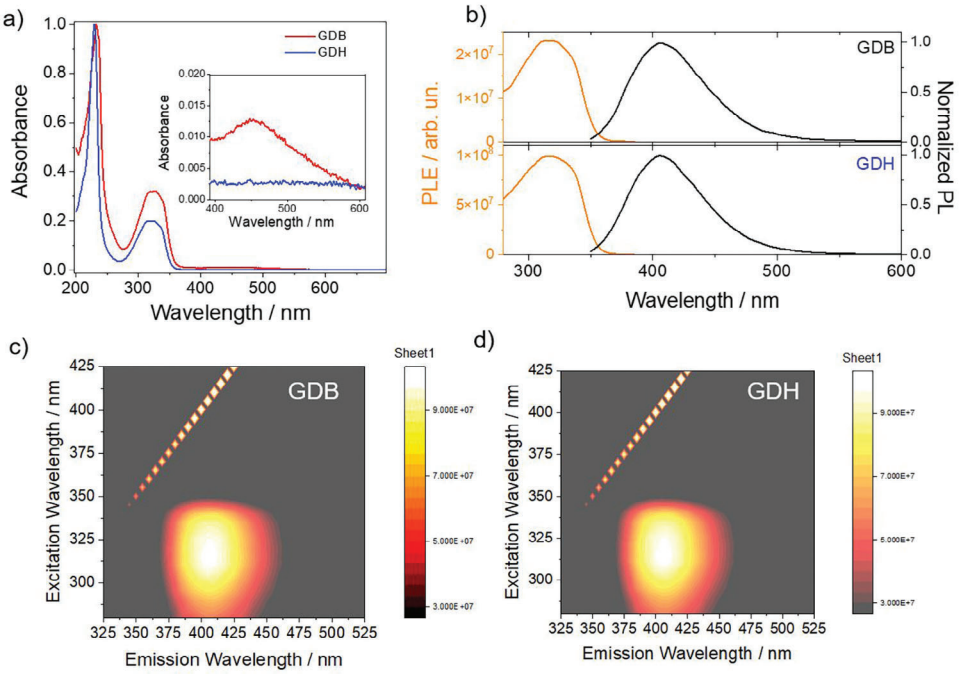

Figure 6. a) UV–Vis spectra of GDB and GDH C-dots. b) Emission (yellow curve) and excitation (black curve) spectra of GDB and GDH C-dots; c) and d) 3D emission-excitation-intensity (false color scale) maps of GDB and GDH samples.

appears inversely proportional to the quantity of C• centers. However, the fact that only GDB shows an increasing of the C• centers containing radicals under irradiation, in particular visible light, clearly indicates that only in these samples the light induces an electronic distribution rearrangement. This change is probably related to the capability to generate singlet oxygen.

The optical properties of the C-dots, as characterized, provide valuable insights that support the interpretation of the EPR results. The UV-Vis spectra of GDH and GDB samples exhibit strong absorptions in the UV, peaking around 235 and 325 nm (**Figure** 6a). These spectra are attributed to the characteristic π–π^* transitions of the naphthalene molecule. Notably, the spectrum of the GDB sample shows an absorption tail that extends into the visible range, reaching down to 600 nm. While the difference in absorbance in the visible range is not substantial, it is still discernible (see the inset in Figure 6a).

When excited between 250 and 350 nm, both GDB and GDH samples show a broad and featureless emission peaking at 410 nm, which is characteristic of the amino-substituted compounds of the naphthalene structure (Figure 6b–d).

The ability to form singlet oxygen when exposed to UV light has been tested using indocyanine green (ICG) in a colorimetric assay. The EPR test to detect singlet oxygen formation, in fact, cannot be done under UV irradiation because the 4-oxo-TEMPO probe photodegrades. On the contrary, ICG is stable under UV and has an absorption band at 780 nm, which decreases in intensity as a result of the formation of $^1O_2$ due to the decomposition of ICG by dioxetane reaction. **Figure** 7a,b shows the absorption decay of ICG dissolved in GDB and GDH aqueous dispersions when irradiated with UV light at 365 nm.

The ICG absorbance in the GDH suspension shows a faster decay rate than in GDB, suggesting that the GDH system is more efficient in producing $^1O_2$ (Figure 7c). Under these conditions, the formation of singlet oxygen follows a different pathway compared to activation by VL. Furthermore, the higher efficiency of GDH suggests that, under UV exposure, a higher number of C• could help the formation of $^1O_2$.

It is evident from the previous chemo-physical characterizations that the reaction between DAN and Gly in a microwave reactor can be used to prepare C-dots with a significant capability to generate singlet oxygen. However, the choice of the acid determines the formation of specific molecular structures that are responsible for distinct responses to light stimulation. When C-dots are exposed to UV light, GDH appears to be more efficient than GDB, while GDB is the only system that responds to VL excitation. These two properties are connected to the different chemical conversion undergoing the DAN molecule during the C-dots formation. In GDH, the DAN reacts almost stoichiometrically with Gly, producing the DAN-Gly_2 derivative.

On the contrary, the GDB C-dots contain poly-DAN macromolecules and these specific compounds are responsible for the absorption tail in the visible range (Figure 6a). The choice of an appropriate catalyst drives the synthesis toward radical-enriched C-dots with a specific photo-activated response, which could be triggered on demand whenever the $^1O_2$ formation is required. The DAN precursor is the main one responsible for these properties. The molecule, in fact, can produce singlet oxygen in solution when excited by UV light (Figure S14, Supporting Information). However, the scarce solubility in water and the relative harmfulness of DAN are limiting the use of this compound in its molecular state. The incorporation of DAN into a carbon nanoparticle improves the solubility in water and buffers. At the same time, the C-dots are not cytotoxic (Figure S15, Supporting Information) and optimize the photoactivity of the molecule. When DAN reacts

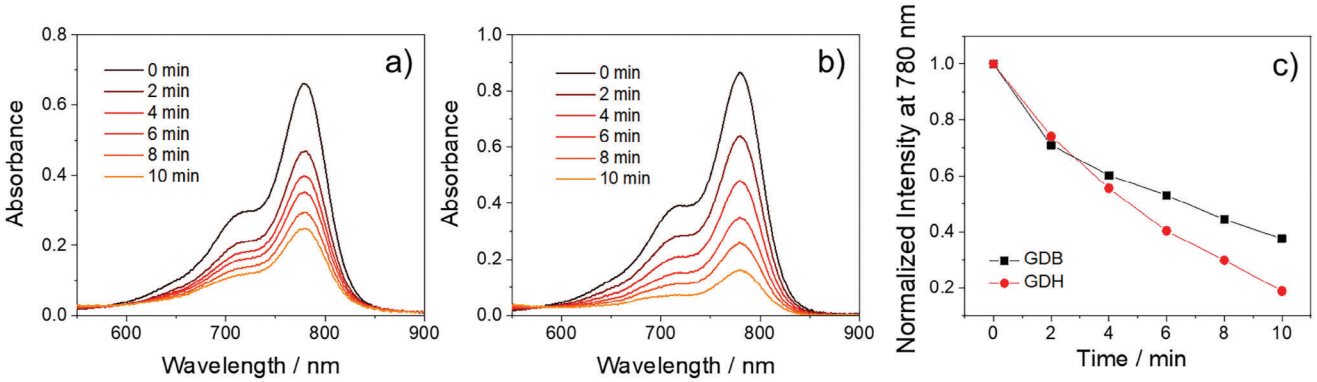

Figure 7. UV–Vis absorption of a GDB a) and GDH b) dispersions containing 0.0027 M of ICG exposed to 365 nm light for increasing times. c) Evolution of the normalized intensity of the ICG peak at 780 nm in the GDB and GDH dispersion when exposed to UV light for increasing times. The lines are guides for the eye.

with glycine to form DAN-Gly_2, it produces more efficiently $^1O_2$ if excited in the UV range.

Previous DAN-based C-dots have already proved to emit singlet oxygen when excited in the UV and no other ROS, such as hydroxyl radicals, superoxide, or hydrogen peroxide, have been detected using specific colorimetric tests.[41] On the basis of those results, the mechanism of singlet oxygen formation must involve the energy transfer from the C-dot, which acts as a sensitizer, to oxygen in the ground triplet state.[9] Moreover, if boric acid is used instead of HCl, the thermal treatment pushes the DAN molecules to polymerize into a poly-DAN structure. We attribute the absorption in the visible range of the GDB C-dots to this compound, which in turn, enables the production of $^1O_2$ under blue light irradiation. Another significant effect that is likely to enhance the formation of single oxygen is a better O_2 absorption capability by the C-dots, in comparison to a single molecule like DAN, which promotes the energy for ROS generation.

2.3. C-dot Antiviral Activity

The potential of using C-dots with the capability of generating singlet oxygen as virucidal agents has been tested toward different variants of SARS-CoV-2 coronavirus. Multiple testing is very important because, in general, it has been observed that the response to vaccines and antivirals greatly changes with the variants of SARS-CoV-2. At first, the tests have been performed by adding the C-dots in buffer solutions with known virion concentration and then exposing the solutions to UV (at 365 nm) and VL (at 450 nm) for 5 min. Solutions incubated in the dark have been used as control. The C-dot concentration in the wells containing the virion solutions has been set at 5 mg mL^{-1} for both the GDH and GDB. This is 50% of the cytotoxic concentration (CC50%), as determined in vitro by checking the cell monolayer integrity of Vero E6 cells exposed to increasing concentrations of C-dots in a medium (Figure S15, Supporting Information).

Figure 8a resumes the results obtained using a sub-optimal exposure time to UV light, causing minimal changes in viral titer, measured as 50% tissue culture infectious dose (TCID50 mL^{-1}). Both types of C-dots exhibit remarkable antiviral activity when exposed to UV light, being capable of completely breaking up the SARS-CoV-2 virions (Original strain) in a short time of exposure. On the contrary, the effect of the C-dots in dark on the virion is negligible, being inside the estimated error bars of the measurements. This suggests that the antiviral activity is not due to the inhibition of replication but to the disruption of the viral

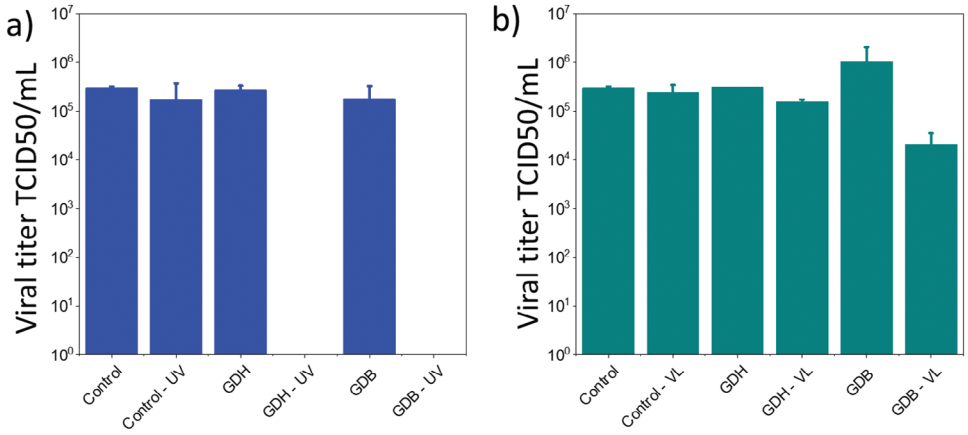

Figure 8. a) Virucidal activity of GDH and GDB C-dots against SARS-CoV-2 original strain after exposure to 365 and 450 nm light for 5 min (a and b, respectively).

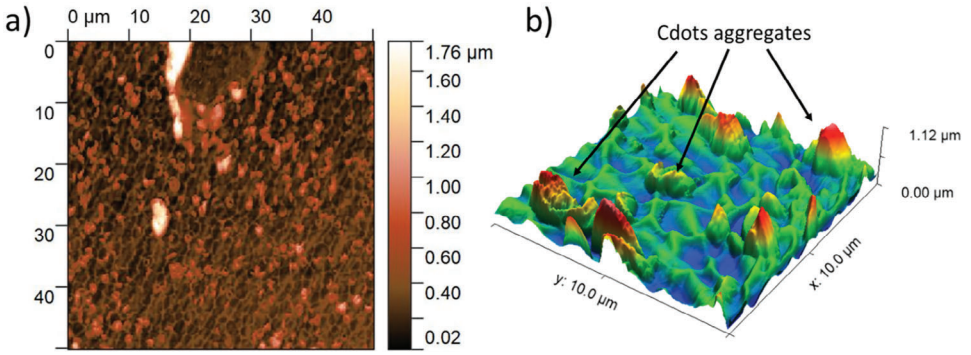

Figure 9. a) AFM image of the amino-functionalized surface after decoration with the GDB C-dots. b) 3D view of the AFM image emphasizing the presence of C-dot aggregates on the surface.

membrane through peroxidation of membrane phospholipids by the photogenerated ROS. The disruption of the viral envelope inhibits the fusion between the virus and the cell membrane. The photoinduced virucidal activity of GDH and GDB samples have been also tested under exposure to VL at 450 nm (Figure 8b). Remarkably, GDH induces a minimal change in viral titer, while in presence of the GDB C-dots, when exposed to visible light, the viral titer falls of ≈ 2 log (corresponding to 2 orders of magnitude). The different antiviral activity of the two C-dots is attributed to the change in the absorbance in the visible range. The GDB sample, in fact, exhibits a broad and faint absorption band peaked at 450 nm (Figure 6a) while the GDH sample does not absorb. The absorbance in the visible can be attributed to the presence of specific organic moieties, such as poly-DAN, in the GDB C-dots. On the contrary, the radicals present in the GDH and in the DAN molecules, although detected in a higher weight concentration with respect to the GDB, are not sensitive to the photon irradiation, both in the UV and visible range (vide supra). This observation also suggests that the chemo-physical phenomena leading to the $^1O_2$ formation and, therefore, the virucidal activity are manifold and related to different mechanisms of energy transfer between the C-dots and the buffer solution.

The virucidal efficacy of GDB under visible light irradiation can be exploited to provide antiviral properties to so-called "high-touch surfaces,", that is, surfaces that are frequently touched with the hands and can be easily contaminated with fomites, contributing to the spread of virus-related diseases.[42] As a proof of concept, we have used a slice of a silicon wafer that has been at first coated with a silica layer, then functionalized with amino groups, and finally decorated with GDB. The C-dots have been chemically anchored via amide bonds by using 1-ethyl-3-(3-dimethylaminopropyl)carbodiimide (EDC) and 1-hydroxypyrrolidine-2,5-dione (NHS) coupling agents.[43] The optical appearance of the coating does not change after C-dots functionalization, indicating the formation of a very thin layer of nanoparticles (Figure S16a, Supporting Information). After the C-dot reaction with the silica surface, the atomic force microscopy (AFM) reveals mainly the presence of sub-micron-sized aggregates randomly distributed on the analyzed area (**Figure 9a,b**). The 3D view of the decorated surface shows that the heights of the biggest C-dots aggregates are smaller than one micron and they appear well separated on a scale of several microns, justifying the absence of changes in optical appearance of the surface. For sake of comparison, we have characterized a second surface that has been left to react with the EDC/NHS coupling agents only, without the addition of C-dots (Figure S16b, Supporting Information). The residual coupling agents form a completely different roughness morphology characterized by micron-scale wrinkles. Although aggregates are visible on most surfaces, when measured at higher AFM magnification, specific areas reveal the presence of small, uniformly-sized particles that match the dimensions of the C-dots as measured by TEM. (Figure S17, Supporting Information).

It is noteworthy that the C-dots remain attached to the surface after several washes with deionized water and even after being subjected to ultrasonication for thirty seconds. This clearly demonstrates that the chemical bond is strong enough to prevent the C-dots from detaching from the substrate.

The decoration with GDB C-dots provides strong antiviral properties to the surface when it is irradiated with UV or even visible light. Spectroscopic tests with ICG exposed to 365 nm light confirm that the C-dots functionalization is responsible for the $^1O_2$ formation, while not-functionalized films do not affect the ICG absorption (Figure S18, Supporting Information). The virucidal performances have been tested using a method similar to that applied to the C-dot suspension, but optimized for the solid surface. A 5 µL viral suspension of known concentration was laid down over small squared pieces of functionalized surface. The surfaces have been at first exposed to UV or visible light, and afterward the residual viral titer has been determined. The virucidal activity of functionalized surfaces has been tested with the original strain and Omicron variant, to check eventual difference in efficacy.

Figure 10 resumes the most effective results of the antiviral tests. In dark condition, the amino-silica-coated surface does not affect the virus titer, confirming that the surface functionalization used to graft the C-dots on the silicon substrate does not interfere with the analysis. On the other hand, as already observed in Figure 8, the UV light exposure affects viral titer in non-functionalized silicon surfaces (Control). The GDB-decorated surfaces exhibit an excellent virucidal effect under exposure to UV, as proved by a reduction of the viral titer of more than 5 logs. The UV irradiation has an excellent antiviral efficacy on both the Original[41] and Omicron[42] variant without noticeable differences. Remarkably, the GDB- functionalization shows a strong efficacy also under VL: this result is more evident

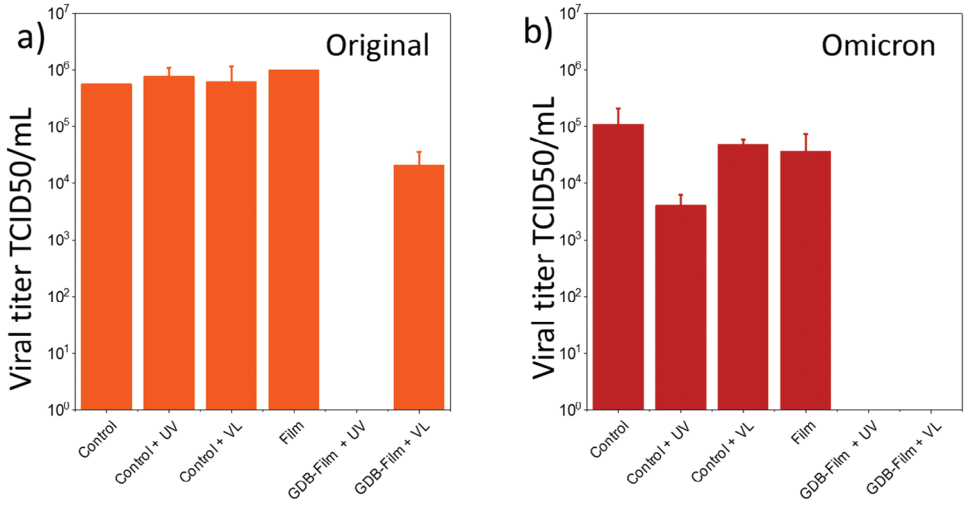

Figure 10. Virucidal activity of GDB-decorated surface measured versus Original and Omicron variants (a and b, respectively) after exposure to 365 (UV) and 450 nm (VL) light.

on the Omicron variant, where the viral titer is reduced down to the detection limit. The Original variant, on the contrary, shows a sensible reduction in the viral titer, which, however, remains at detectable levels. A decrease of more than two orders of magnitude in the viral concentration (2 logs) is observed, corresponding to a reduction of more 99% of the initial value. It is possible to state that the GDB C-dots confer an extraordinary antiviral effect on the surface, promoted by exposure to light, both in the UV and visible range.

3. Conclusion

Preparing C-dots with specific functional properties requires careful design of the material, tailoring the properties according to use. Therefore, manufacturing C-dots with oxidant properties, such as being able to be used as antivirals, needs an accurate selection of the right precursors and synthesis process. In the present work, we have demonstrated that it is possible to use microwave reactor synthesis to obtain C-dots with antiviral properties starting from an amino acid, glycine, and a molecule containing aromatic groups, 1,5-diaminonaphthalene. A key step in the synthesis is the selection of an appropriate acid catalyst, without which the reaction between the two precursors cannot take place. The use of boric acid or hydrochloric acid as catalysts produces C-dots having different molecular structures while starting from the same precursors. HCl as a catalyst promotes the formation of copolymers, while H_3BO_3 induces homopolymerization of the precursors, with the formation of poly-DAN macromolecules and Gly structures of smaller extent.

Despite these differences, both types of C-dots show the presence of C• centers, although to different extents. The formation of C• species in GDB dots increases upon irradiation by UV light and to a lesser degree when exposed to visible light. Conversely, GDH dots do not respond to UV or visible light illumination. Remarkably, both C-dots exhibit efficient ROS emission when irradiated with UV light, as confirmed by colorimetric assays and measurement of magnetic properties. However, only the boric acid-catalyzed C-dots show a significant response to visible light irradiation, considering the variation of C• in the solid state and the formation of singlet oxygen. Another interesting finding is that GDH appears to be more efficient than GDB to generate ROS when exposed to UV light but GDB is the only system that responds to visible light excitation.

The formation of ROS and radical species, indicates that the C-dots can be potential antiviral systems capable of disrupting the virion structure. When used as a virucidal agent in solution, C-dots achieve complete virus inactivation within a time range of 5 min. A remarkable result is the antiviral performance of the GDB dots when photoactivated by visible blue light. The C-dots can also be used to create photoactive antiviral surfaces. The grafting of the C-dot surface via chemical amide bonding allows obtaining nanoparticles modified to be attached to different types of surfaces without altering the optical appearance of the surfaces to be functionalized. The performance of GDB-decorated silicon wafers as proof-of-concept virucidal surfaces confirms that this emerging class of nanoparticles is a valuable asset in the fight against the spread of viral diseases and future pandemics.

Indeed, the use of a safe photon wavelength for the production of light-activated antiviral ROS is an important breakthrough in the field of large-scale sanitization of high-contact surfaces, such as door handles or light switches, especially in critical environments such as hospitals or hospices.

4. Experimental Section

Chemicals: Glycine (Gly, purity 98.5%), boric acid (purity 99.5%), and glycerol (purity 99.5%) were purchased from Carlo Erba Reagents. 1,5-diaminonaphthalene (DAN, purity 97%), tetraethoxysilane (TEOS, purity 98%), 3-aminopropyl-triethoxysilane (APTES, purity 99%), hydrochloric acid (37%), 1-ethyl-3-(3-dimethylaminopropyl)carbodiimide (EDC), 1-hydroxypyrrolidine-2,5-dione (NHS), sodium 4-[2-[(1E,3E,5E,7Z)−7-[1,1-dimethyl-3-(4-sulfonatobutyl)benzo[e]indol-2-ylidene]hepta-1,3,5-trienyl]−1,1-dimethylbenzo[e]indol-3-ium-3-yl]butane-1-sulfonate (indocyanine green), 2,2,6,6-tetramethyl-4-piperidone (4-oxo-TEMPH) and ethanol (concentration ≥99.5% v/v) were purchased from Sigma Aldrich. All the chemicals were used without any further purification. Milli-Q water

was used for synthesis and analysis. P-type, B-doped silicon wafers, with a thickness of 350 µm, were purchased from Si-Mat and used as the substrate for surface functionalization. The silicon wafer was ultrasonicated for 2 h in a HCl 1 M water solution and then rinsed with ethanol before using.

Viral Isolate: The human 2019-nCoV strain 2019-nCoV/Italy-INMI1, named Original strain,[44] and the Omicron variant BA.1,[45] named Omicron, were kindly provided by the from Istituto Lazzaro Spallanzani (Rome, Italy) and the Department of Molecular and Translational Medicine, Section of Microbiology and Virology, University of Brescia Medical School, (Brescia, Italy).

C-dots Synthesis and Purification: Two types of C-dots were prepared using an acid-catalyzed reaction in the presence of hydrochloric or boric acid. The samples were named GDH and GDB, respectively.

At first, Gly and DAN were solubilized in milli-Q water in the molar ratio 1:1, using the following amount: 0.15 g of glycine and 0.31 g of 1,5-diaminonaphthalene, in 20 mL of milli-Q water. After solubilization, the hydrochloric acid and the boric acid were added in the molar ratios: Gly:DAN:HCl = 1:1:0.2 and Gly:DAN:H_3BO_3 = 1:X:1, with X = 0.1, 0.5 and 1. The acronym "GDB_X" indicates the GDB C-dots with a X DAN molar ratio; if it is not further specified, GDB is the Gly/DAN ratio of 1.

After the acid addition, the aqueous solutions were ultrasonicated for 5 min and then treated at 1000 W for 3 min in a commercial microwave oven. A dark powder was the final product. The powder was further solubilized in 20 mL of milli-Q water, filtered through a cellulose acetate syringe filter with a pore size of 0.22 µm (Whatman Puradisc 30), and finally placed inside a benzoylated dialysis membrane with a cut-off of 2000 Daltons (Sigma Aldrich) and dialyzed with a tube against milli-Q water for 24 h, changing the water every 2 h. Finally, dialyzed solutions were poured into a silicone mold and placed in an oven in the air at 60 °C for 14 h to remove the solvent.

Materials Characterization: UV–vis spectra were measured in absorbance mode from 200 to 600 nm by using a Nicolet Evolution 300 UV–vis spectrophotometer (Thermo Fisher). A concentration of 0.8 mg mL^{-1} C-dots dispersed in water was used for the analysis. For colorimetric single oxygen detection, 60 µL of a 0.0027 M Indocyanine green aqueous solution was added to a 2 mL of 0.8 mg mL^{-1} aqueous solution of C-dots.

Zolix LED power supply, equipped with LED light sources model M365L and M450L, was used to irradiate the solution at 365 and 450 nm, respectively. Each sample was irradiated for 2 min at 20 mW cm^{-2} before UV–vis acquisition of the Indocyanine green absorption maximum at 785 nm.

X-ray diffraction (XRD) patterns were recorded using a Bruker diffractometer D8 Discover working in grazing incidence geometry with a Cu K_α line (λ = 1.54056 Å). The X-ray generator was set at 40 kV and 40 mA. Diffraction patterns were recorded in 2θ ranging from 10 to 60° with a step size of 0.05° and a scan speed of 0.5 s/step for 4 h.

Absorption Fourier-transform infrared (FTIR) spectra were recorded by a Vertex 70 interferometer (Bruker) in the 4000–400 cm^{-1} range with a 4 cm^{-1} resolution and 32 scans. The spectra were recorded using KBr pellets with 1 mg of sample and 500 mg KBr.

Fluorescence analysis of the samples solubilized in water was done using a Horiba Jobin Yvon NanoLog spectrofluorometer with an excitation and emission wavelength ranging from 300 to 700 nm. A concentration of 0.1 mg mL^{-1} was used for the analysis.

X-ray photoelectron spectroscopy (XPS) was carried out in a custom-designed UHV system equipped with an EA 125 Omicron electron analyzer with five channeltrons, working at a base pressure of 10–10 mbar. Core level photoemission spectra (C 1s and N 1s) were collected in normal emission at room temperature with a non-monochromatized Al Kα X-ray source (1486.7 eV), and using 0.1 eV steps, 0.5 s collection time and 20 eV pass energy.

Transmission electron microscopy (TEM) images were acquired with a Jeol JEM 1400 Plus and on a Hitachi H-7000 microscope. Once dispersed in a tiny amount of ethanol, the samples were drop-casted on a carbon-coated copper grid and left to evaporate at room temperature. ImageJ software was used to analyze the TEM pictures.

Atomic Force Microscopy (AFM) was performed with a microscope NT-MDT Ntegra at 0.8 Hz scan speed in semicontact mode, using a silicon tip with the nominal resonance frequency of 150 kHz, 5 N m^{-1} force constant, and 10 nm typical curvature radius.

Nuclear Magnetic Resonance (NMR) spectra were collected using a Bruker (Bruker Biospin, Karlsruhe, Germany) Avance spectrometer, equipped with a 5-mm multinuclear inverse detection probe BBI, in deuterated dimethyl sulfoxide (99.8%, Cambridge Isotope Laboratories Inc., Andover, MA, USA) at frequencies of 600.13 and 150.90 MHz for ^{1}H and ^{13}C NMR, respectively. 1D proton spectra were acquired with a 90° pulse of 10.95 µs and 64 scans. In the ^{1}H-^{13}C Heteronuclear Single Quantum Coherence (HSQC) and Heteronuclear Multiple Bond Correlation (HMBC) experiments, which were all gradient-selected experiments, a total of 256 spectra, each containing 2048 or 4096 data points, respectively, were accumulated. For acquiring the HSQC, a sensitivity-improved double-inept transfer, phase-sensitive sequence was used with decoupling during acquisition and gradients in back-inept, 32 scans and 16 dummy scans, J(^{13}C-^{1}H) = 145 Hz and spectral window of 7k × 33 201 Hz. The HMBC sequence was optimized with long-range couplings (J = 10 and 145 Hz) and suppression of one-bond correlations with low-pass J-filters, 32 scans and 16 dummy scans were acquired, over the same spectral windows used for HSQC. 2D homonuclear shift correlation was performed by using a COSY sequence with gradient pulses for selection, acquiring 256 spectra of 2048 data points, 16 scans and 16 dummy scans, and spectral windows of 7002 × 6999 Hz. All NMR experiments were carried out at 298 K (Bruker BVT3000 and BCU05 units, Bruker Biospin, Karlsruhe, Germany) and using a relaxation delay of 3 s.

Solid state Electron Paramagnetic Resonance (EPR) spectra were acquired using a Bruker EMX spectrometer operating at X-band (9.5 GHz), equipped with a cylindrical cavity operating at 100 kHz field modulation. All the spectra were recorded at room temperature (RT) with a 10 mW of incident microwave power. Experiments were carried out both in a static vacuum, obtained by connecting Suprasil quartz glass cells to a high vacuum pumping system (residual pressure P < 10^{-3} mbar), and in the presence of O_2 at the pressure of 20 mbar. In situ irradiations were performed using a UV LED centered at 365 nm and a blue LED centered at 470 nm, setting the power to have the same irradiance value of 250 W m^{-2} for both types of light.

To detect the formation of singlet oxygen, 3 mg mL^{-1} aqueous suspensions of the samples buffered at basic pH and containing the molecule 4-oxo-TEMPH (0.044 M) were prepared. This molecule can react with singlet oxygen to form the paramagnetic adduct 4-oxo-TEMPO. The photogeneration of the adduct was followed by acquiring EPR spectra on a benchtop EPR spectrometer (ADANI's SPINSCAN X) after 5, 15, and 30 min of ex situ irradiation with a 470 nm LED.

Antiviral Surface Synthesis: Silicon wafers were used as substrates for the preparation of an antiviral layer. The wafers were cut into 1.5 × 3 cm parts, washed with ethanol, and dried in an oven in the air at 60 °C for 1 h. The synthesis was divided into three parts: a) deposition of a silica layer onto the silicon substrate, b) functionalization of the surface with amino groups, and c) C-dots grafting.

In the first step, a silica precursor sol was prepared to deposit a thin film on the substrates. The sol was obtained by adding 10 mL of TEOS to 15 mL of ethanol (EtOH) and 2.5 mL of 1 M HCl. Before deposition, the sol was placed under stirring for 90 min at room temperature. The silicon substrates were dip-coated in the solution with a 100 mm min^{-1} withdrawal rate and then treated at 350 °C for 2 h.

The silica layers were chemically functionalized to expose the amino groups on the surface. A sol made of 5 mL of APTES, 20 mL of EtOH, and 1.5 mL of 1 M HCl was placed under stirring for 1 h at room temperature. Then, the substrates covered by the silica films were immersed in the APTES sol and dip-coated with a withdrawal rate of 100 mm min^{-1} and finally treated at 120 °C for 1 h.

An EDC/NHS coupling reaction was performed to graft C-dots on the amine-modified silica surface: 200 mg C-dots, 200 mg of EDC, and 120 mg of NHS were solubilized in 10 mL of DMF (N,N-dimethylformamide). The amino-functionalized films were immersed into the solution and heated

at 70 °C for 24 h under stirring. Afterward, the samples were rinsed with water and dried in an oven in the air at 60 °C for 1 h.

Cytotoxicity Assessment: Cytotoxicity of the C-dots was evaluated using Vero E6 cells (Cercopithecus aethiops, kidney, ATCC CRL-1586) as a reference. The cell line was routinely maintained in a Dulbecco Modified Eagle Medium (DMEM) supplemented with 1% glutamine, 1% penicillin/streptomycin, and 10% fetal bovine serum. After the cells were grown, they were placed inside a 96-well plate and grown for another 24 h to achieve optimal cell density. After this period, the cells were subjected to different concentrations of the nanomaterial and were left to incubate for 72 h. The measurement was performed in triplicate. The cytotoxic effect was evaluated through microscopy observation (determination of cell monolayer integrity). A cytotoxic concentration of 50% (CC50, concentration resulting in 50% loss of cell viability compared to untreated control) was calculated.

Virucidal Activity: The virucidal activity was evaluated by modifying the guidelines given in the standard for testing chemicals as disinfectants.[46] A volume of the viral suspension of SARS-CoV-2 (both Original strain and Omicron variants) was put on a 96-well plate lid (12 × 8 cm). A volume of C-dots in buffer was added to the viral suspension (final volumes and concentrations are indicated in the results section).

Alternatively, TEOS-APTES plates functionalized with the test nanomaterial were used for testing virucidal activity. Suspensions or plates were then left in the dark or exposed to visible (450 nm) or ultraviolet light (365 nm) for the time indicated in each experiment (range 5–10 min). Zolix LED power supply, equipped with LED light sources model M365L and M450L, was used to irradiate the wells at a power of 20 mW cm^{-2} and at a distance of ≈ 10 cm. A culture medium was used as control, added to the viral suspension, and exposed to the dark or to visible/ultraviolet light as with nanomaterials. After an additional 5-min incubation, viral suspensions were collected, and viral titer was determined. Vero E6 cells were cultured in 96-well plate (20.000 cells per well). After 24 h cells were infected with serial dilutions of each collected treated or untreated viral sample (from 10^{-2} to 10^{-5}) in 6-well replicates. After three additional days, infection was determined by observation of the cytopathic effect in each test well. Infection data were employed to calculate viral titer according to Reed and Muench's methodology.[47]

Supporting Information

Supporting Information is available from the Wiley Online Library or from the author.

Acknowledgements

This work was funded and developed within the framework of the project e.INS—Ecosystem of Innovation for Next Generation Sardinia (grant number ECS 00000038), funded by the Italian Ministry for Research and Education (MUR) under the National Recovery and Resilience Plan (NRRP)—MISSION 4 COMPONENT 2, "From research to business" INVESTMENT 1.5, "Creation and strengthening of Ecosystems of innovation", and construction of "Territorial R&D Leaders". The authors acknowledge the CeSAR (Centro Servizi Ricerca d'Ateneo) core facility of the University of Cagliari and Dr. Andrea Ardu for assistance with the generation of TEM images. Fondazione Centro Servizi alla Persona is acknowledged for the financial support.

Conflict of Interest

The authors declare no conflict of interest.

Author Contributions

L.S. L.M. and P.I. conceptualized the idea for study, reviewed and edited the final manuscript. L.S., M.P., D.C., L.M., and P.I. wrote the original draft. L.S., M.P., L.M., and P.I. designed methodology; L.S., M.P., D.C., D.D.F., M.F.C., B.P, F.L., S.L., A.Z., and L. C. performed investigation and data curation. L.S., M.P., D.C., D.D.F., M.F.C., S.L., A.Z., and L. C. performed formal analysis. All authors have read and agreed to the submitted version of the manuscript.

Data Availability Statement

The data that support the findings of this study are available from the corresponding author upon reasonable request.

Keywords

antivirals, carbon dots, photocatalyst, singlet oxygen

Received: March 14, 2024
Revised: May 14, 2024
Published online:

[1] S. Hebbar, E. Knust, *BioEssays* **2021**, *43*, 2100096.
[2] N. Tyagi, K. Gambhir, S. Kumar, G. Gangenahalli, Y. K. Verma, *J. Mater. Sci.* **2021**, *56*, 16790.
[3] H. J. Shields, A. Traa, J. M. Van Raamsdonk, *Front. Cell Dev. Biol.* **2021**, *9*, 628157.
[4] P. Innocenzi, L. Stagi, *Nano Today* **2023**, *50*, 101837.
[5] P. R. Ogilby, *Chem. Soc. Rev.* **2010**, *39*, 3181.
[6] A. K. Gill, S. Shah, P. Yadav, A. Shanavas, P. P. Neelakandan, D. Patra, *J. Mater. Chem. B* **2022**, *10*, 9869.
[7] W. Hao, C. Zhao, G. Li, H. Wang, T. Li, P. Yan, S. Wei, *Environ. Pollut.* **2023**, *322*, 121195.
[8] N. Peng, Y. Du, G. Yu, C. Zhang, Q. Cai, H. Tang, Y. Liu, *Langmuir* **2022**, *38*, 13139.
[9] R. Canaparo, F. Foglietta, T. Limongi, L. Serpe, *Materials* **2021**, *14*, 53.
[10] P. Straková, P. Bednář, J. Kotouček, J.í Holoubek, A. Fořtová, P. Svoboda, M. Štefánik, I. Huvarová, P. Šimečkov, J. Mašek, D. A. Gvozdev h, I. E. Mikhnovets, A. A. Chistov, T. D. Nikitin, M. S. Krasilnikov, A. V. Ustinov, V. A. Alferova, V. A. Korshun, D. Růžek, L. Eyer, *Virus Res.* **2023**, *334*, 199158.
[11] J. Holoubek, J. Salát, J. Kotouček, T. Kastl, M. Vancová, I. Huvarová, P. Bednář, K. Bednářov, D. Růžek, D. Renčiuk, L. Eyer, *Antivir. Res.* **2024**, *221*, 105767.
[12] M. C. Wolf, A. N. Freiberg, T. Zhang, Z. Akyol-Ataman, A. Grock, P. W. Hong, J. Li, N. F. Watson, A. Q. Fang, H. C. Aguilar, M. Porotto, A. N. Honko, R. Damoiseaux, J. P. Miller, S. E. Woodson, S. Chantasirivisal, V. Fontanes, O. A. Negrete, P. Krogstad, A. Dasgupta, A. Moscona, L. E. Hensley, S. P. Whelan, K. F. Faull, M. R. Holbrook, M. E. Jung, B. Lee, *Proc. Natl. Acad. Sci. USA* **2010**, *107*, 3157.
[13] P. Innocenzi, L. Stagi, *Chem. Sci.* **2020**,*11*, 6606.
[14] J. Ren, L. Stagi, P. Innocenzi, *Prog. Solid State Chem.* **2021**, *62*, 100295.
[15] Y. Liu, S. Roy, S. Sarkar, J. Xu, Y. Zhao, J. Zhang, *Carbon Energy* **2021**, *3*, 795.
[16] M. Azami, J. Wei, M. Valizadehderakhshan, A. Jayapalan, O. O. Ayodele, K. Nowlin, *J. Phys. Chem. C* **2023**, *15*, 7360.
[17] H. Ding, X.-H. Li, X.-B. Chen, J.-S. Wei, X.-B. Li, H.-M. Xiong, *J. Appl. Phys.* **2020**, *127*, 231101.
[18] V. Pouchaname, R. Madivanane, A. Tinabaye, **2012**, *584*, 371
[19] S. Rodríguez-Varillas, T. Fontanil, Á. J. Obaya, A. Fernández-González, C. Murru, R. Badía-Laíño, *Appl. Sci.* **2022**, *12*, 773.
[20] T. A. Tabish, C. J. Scotton, D. C. J. Ferguson, L. Lin, A. Van Der Veen, S. Lowry, M. Ali, F. Jabeen, P. G. Winyard, S. Zhang, *Nanomedicine* **2018**, *13*, 1923.

[21] L. Stagi, D. De Forni, L. Malfatti, F. Caboi, A. Salis, B. Poddesu, G. Cugia, F. Lori, G. Galleri, P. Innocenzi, *Nanoscale* **2021**, *13*, 16465.
[22] F. Fiori, F. L. Cossu, F. Salis, D. Carboni, L. Stagi, D. De Forni, B. Poddesu, L. Malfatti, A. Khalel, A. Salis, M. F. Casula, R. Anedda, F. Lori, P. Innocenzi, *Nanomaterials* **2023**, *13*, 3090.
[23] A. Rateb, Z. Ghubish, A. F. Abdel, M. El-kemary, *J. Photochem. Photobiol. A Chem.* **2023**, *443*, 114867.
[24] X.-D. Tang, H.-M. Yu, W. Nguyen, E. Amador, S.-P. Cui, K. Ma, M.-L. Chen, S.-Y. Wang, Z.-Z. Hu, W. Chen, *Adv. Photonics Res.* **2023**, *4*, 2200314.
[25] Q. Zhang, R. Wang, B. Feng, X. Zhong, K. (Ken) Ostrikov, *Nat. Commun.* **2021**, *12*, 1.
[26] Y. Zhou, H. Sun, F. Wang, J. Ren, X. Qu, *Chem. Commun.* **2017**, *53*, 10588.
[27] F. L. Cossu, M. Poddighe, L. Stagi, R. Anedda, P. Innocenzi, *Macromol. Chem. Phys.* **2022**, *223*, 22000052.
[28] J. Coates, *Interpretation of Infrared Spectra, A Practical Approach*, Wiley, New York **2006**.
[29] N. Sharma, U. Kumar Sharma, R. Kumar, R. A. K. Sinha, *RSC Adv.* **2012**, *2*, 10648.
[30] M. A. Azzem, U. S. Yousef, D. Limosin, G. Pierre, *J. Electroanal. Chem.* **1996**, *417*, 163.
[31] S. Arkhipenko, M. T. Sabatini, A. S. Batsanov, V. Karaluka, T. D. Sheppard, H. S. Rzepa, A. Whiting, *Chem. Sci.* **2018**, *9*, 1058.
[32] M. Kehrer, J. Duchoslav, A. Hinterreiter, M. Cobet, A. Mehic, T. Stehrer, D. Stifter, *Plasma Process Polym.* **2019**, *16*, 1800160.
[33] J. Ederer, P. Janoš, P. Ecorchard, J. Tolasz, V. Štengl, H. Beneš, M. Perchaczc, O. Pop-Georgievski, *RSC Adv.* **2017**, *7*, 12464.
[34] V. Vaz da Cruz, R. Büchner, M. Fondell, A. Pietzsch, S. Eckert, A. Föhlisch, *J. Phys. Chem. Lett.* **2022**, *13*, 2459.
[35] T. Wang, J. S. Stevens, T. Vetter, G. F. S. Whitehead, I. J. Vitorica-Yrezabal, H. Hao, A. J. Cruz-Cabeza, *Cryst. Growth Des.* **2018**, *18*, 6973.
[36] B. L. Grigorenko, M. G. Khrenova, A. V. Nemukhin, *Phys. Chem. Chem. Phys.* **2018**, *20*, 23827.
[37] C. Gil-Lozano, A. G. Fairén, V. Muñoz-Iglesias, M. Fernández-Sampedro, O. Prieto-Ballesteros, L. Gago-Duport, E. Losa-Adams, D. Carrizo, J. L. Bishop, T. Fornaro, E. Mateo-Martí, *Sci. Rep.* **2020**, *10*, 15097.
[38] L. Tian, C. P. Koshland, J. Yano, V. K. Yachandra, I. T. S. Yu, S. C. Lee, D. Luca, *Energy Fuels* **2009**, *23*, 2523.
[39] I. Corazzari, S. Livraghi, S. Ferrero, E. Giamello, B. Fubini, I. Fenoglio, *J. Mater. Chem.* **2012**, *22*, 19105.
[40] A. Zollo, S. Livraghi, E. Giamello, A. Cioni, V. Dami, G. Lorenzi, G. Baldi, S. Agnoli, M. Adam Baluk, A. Gołąbiewska, A. Zaleska-Medynska, *J. Environ. Chem. Eng.* **2023**, *11*, 111523.
[41] X. Nie, C. Jiang, S. Wua, W. Chen, P. Lv, Q. Wang, J. Liu, C. Narh, X. Cao, R. A. Ghiladi, Q. Wei, *J. Photochem. Photobiol.: Biol.* **2020**, *206*, 111864.
[42] https://www.cdc.gov/healthcare-associated-infections/hcp/cleaning-global/appendix-c.html.
[43] M. J. E. Fischer, In *Surface Plasmon Resonance. Methods in Molecular Biology*, Vol. *627* (Eds: N. Mol, E. Fischer), Humana Press, Totowa, NJ **2010**, pp.55–73.
[44] M. R. Capobianchi, M. Rueca, F. Messina, E. Giombini, F. Carletti, F. Colavita, C. Castilletti, E. Lalle, L. Bordi, F. Vairo, E. Nicastri, G. Ippolito, C. E. M. Gruber, B. Bartolini, *Clin. Microbiol. Infect.* **2020**, *26*, 954.
[45] J. M. Labriola, S. Miersch, G. Chen, C. Chen, A. Pavlenco, R. Saberianfar, F. Caccuri, A. Zani, N. Sharma, A. Feng, D. W. Leung, A. Caruso, G. Novelli, G. K. Amarasinghe, S. S. Sidhu, *ACS Chem. Biol.* **2022**, *17*, 1978.
[46] *European Committee for Standardization (CEN) EN 14476:2013+A2:2019: Chemical Disinfectants and Antiseptics—Quantitative Suspension Test for the Evaluation of Virucidal Activity in the Medical Area—Test Method and Requirements (Phase 2/Step 1) European Committee for Standardization, Brussels, Belgium, 2019.*
[47] L. J. Reed, H. Muench, *Am. J. Epidemiol.* **1938**, *27*, 493.